High Power Laser Science and Engineering, (2019), Vol. 7, e40, 8 pages.

doi:10.1017/hpl.2019.30

A demonstration of extracting the strength and wavelength of the magnetic field generated by the Weibel instability from proton radiography

Bao Du[1], Hong-Bo Cai[1,2,3], Wen-Shuai Zhang[1], Shi-Yang Zou[1], Jing Chen[1,2,3], and Shao-Ping Zhu[1,4,5]

[1]*Institute of Applied Physics and Computational Mathematics, Beijing 100094, China*

[2]*HEDPS, Center for Applied Physics and Technology, Peking University, Beijing 100871, China*

[3]*IFSA Collaborative Innovation Center, Shanghai Jiao Tong University, Shanghai 200240, China*

[4]*STPPL, Research Center of Laser Fusion, China Academy of Engineering Physics, Mianyang 621900, China*

[5]*Graduate School, China Academy of Engineering Physics, Beijing 100088, China*

(Received 31 January 2019; revised 17 April 2019; accepted 4 June 2019)

Abstract

The Weibel instability and the induced magnetic field are of great importance for both astrophysics and inertial confinement fusion. Because of the stochasticity of this magnetic field, its main wavelength and mean strength, which are key characteristics of the Weibel instability, are still unobtainable experimentally. In this paper, a theoretical model based on the autocorrelation tensor shows that in proton radiography of the Weibel-instability-induced magnetic field, the proton flux density on the detection plane can be related to the energy spectrum of the magnetic field. It allows us to extract the main wavelength and mean strength of the two-dimensionally isotropic and stochastic magnetic field directly from proton radiography for the first time. Numerical calculations are conducted to verify our theory and show good consistency between pre-set values and the results extracted from proton radiography.

Keywords: magnetic field; plasma diagnostics; proton radiography; Weibel instability

1. Introduction

The Weibel instability, which is mainly characterized as being able to generate strong magnetic fields, is of great significance for a range of scenarios in plasma physics, and has been studied for many decades since it was first proposed[1–4]. For example, in astrophysics, the magnetic field generated in the Weibel instability is believed to be the leading mechanism for shock formation in weakly magnetized plasmas[5, 6]. While in inertial confinement fusion, the magnetic field generated by the Weibel instability is found to play an important role in the transport of fast electrons and the thermal isotropization of energy flows[7–11].

The classical Weibel instability, which is referred as the thermal anisotropy-driven Weibel instability, arises from electron thermal anisotropy and can increase when a plasma slab is expanding into the vacuum[12]. Besides, the Weibel instability can also be driven by an ion flow, which includes a counterstreaming ion flow but a collisional and isotropic electron population, referred as the ion-driven Weibel instability[13]. Both kinds of instability could result in current filaments longitudinal to the electron or ion flow, and toroidal magnetic fields around the current filaments[14, 15]. The strength and spatial wavelength in the transversal plane of the magnetic field are key parameters for the estimation of other important processes, such as shock formation and electron transport, and are often seen as direct characteristics for judgment of the growth stage of the Weibel instability[15].

Experimentally, when space charge effects between the current filaments have a negligible impact on deflection of the probe proton, which has been proved using the difference in deflection between the electric field and the magnetic field, the magnetic field generated by the Weibel instability can be transversely imaged by proton radiography[16–18]. The emergence of the Weibel instability is then manifested as striations on the proton images. The amount and spatial wavelength of the proton flux striations, which are related to the amount and spatial wavelength of the current filaments, are used to indicate the evolution of the instability,

Correspondence to: H.-B. Cai and S.-P. Zhu, Institute of Applied Physics and Computational Mathematics, Beijing 100094, China. Email: Cai_hongbo@iapcm.ac.cn (H.-B. Cai) and Zhu_shaoping@iapcm.ac.cn (S.-P. Zhu)

such as growth, saturation and coalescence of the current filaments[3, 18].

However, the strength and spatial wavelength of such an isotropic and stochastic magnetic field still cannot be directly inferred from the experiments, as far as we are aware of. The reason for this is given below. The toroidal magnetic fields have an almost constant amplitude along the longitudinal direction; their transversal distribution, however, is two-dimensionally isotropic and stochastic[14]. When a probe proton passes through the plasma, the deflection distance is decided by the path integral of the stochastically distributed magnetic field, i.e., $\int \boldsymbol{B}\,\mathrm{d}l$. The magnetic field vector is neutralized by itself during the integration. Instead of being able to extract the strength and spatial wavelength of the magnetic field, the striations on the detected proton images actually only help in giving the averaged result of the stochastic magnetic field vector along the path of the proton probe.

In proton radiography of three-dimensionally isotropic and stochastic magnetic field turbulence, the mean strength and the main spatial wavelength of the magnetic turbulence can be inferred by extracting the energy spectrum of the magnetic energy $E_B(k)$ from the detected proton flux distribution[19–21]. It has been verified by numerical demonstrations and used to evidence dynamo amplification of magnetic fields in a turbulent plasma[22]. Nevertheless, this method, which requires three-dimensional isotropy, is not suitable for the detection of the Weibel-instability-generated magnetic field, since it is usually developed on the basis of anisotropy of the plasma[12].

In this paper, by theoretically analyzing proton radiography of a two-dimensionally isotropic and stochastic magnetic field, a relationship is built between the proton flux density perturbation on the detection plane and the energy spectrum of the magnetic field. We demonstrate for the first time that the mean strength and main spatial wavelength of the Weibel-instability-generated magnetic field can be inferred by means of proton radiography. Numerical calculations based on ray tracing methods are also conducted to verify our theory.

2. Proton radiography

The Weibel-instability-generated magnetic field has been investigated previously by many particle-in-cell simulations and experiments[3–13, 16–18]. It is shown that when the Weibel instability is excited, current filaments emerge along the longitudinal direction, i.e., the y direction in our coordinate system[3]. The distribution of the center positions of these current filaments is two-dimensionally isotropic and stochastic in the transversal plane, i.e., the x–z plane. Magnetic fields are distributed around each current filament, and are azimuthally directed, i.e., $\boldsymbol{B} = \boldsymbol{B}_\varphi = \boldsymbol{B}_x + \boldsymbol{B}_z$. The longitudinal component $\boldsymbol{B}_y$ is small, and can be ignored. Compared to its transversal distribution, the magnetic field maintains a constant amplitude along the longitudinal direction, composing a tube-like structure around each current filament[8–12]. Because of the spatial distribution of the current filaments, the Weibel-instability-generated magnetic field is also two-dimensionally isotropic and stochastic[14]. Meanwhile, studies also show that after saturation of the Weibel instability, the magnetic field is quasi-static[23].

In proton radiography of a magnetic field or an electric field, the proton probe will be deflected by the field and acquire a deflection velocity after it passes. The spatial distribution of the deflection velocity on exiting the field region is an important parameter. It creates a relationship between the proton flux density obtained on the detection plane and the field to be probed. Furthermore, it has also been proved to be helpful in field reconstruction from the proton flux density in previous studies[24, 25].

Assuming that the deflection distance of the proton probe inside the plasma is small and negligible, when a parallel proton beam has passed through the magnetic field region along the z direction, the deflection velocity on exiting the field region can be approximated as

$$\boldsymbol{u} \approx u_y \boldsymbol{e}_y \approx \frac{q}{\gamma m_p} \int_0^{l_z} B_x \,\mathrm{d}z \boldsymbol{e}_y, \tag{1}$$

where q is the proton charge, m_p is the proton mass, γ is the proton relativistic factor and l_z is the length of the magnetic field region in the z direction. Actually, as well as the emergence of u_y, which comes from the coupling between B_x and u_z, a deflection velocity in the x direction, u_x, can also arise due to the coupling between u_y and B_z. It is later proved by the numerical calculations in Section 4 that u_x is several orders of magnitude lower than u_y, and is ignored in our analyses.

After leaving the field region and traversing a distance L_D in free space, the proton probe will be deposited on the detection plane. The spatial distribution of the deflection velocity finally introduces a perturbation to the spatial density distribution of the proton probe, which will become visible on the detection plane if L_D is large enough. The density perturbation is defined as $\delta n/n_0 = n/n_0 - 1$, where n and n_0 are the proton flux densities on the detection plane when the magnetic field is present and absent, respectively. When the density perturbation satisfies the linear requirement $\delta n/n_0 < 1$, the trajectory crossing or overlapping between the protons would not happen under the chosen spatial resolution. The linearized continuity equation $\delta n/n_0 = -\partial d/\partial y$ is then satisfied, where d is the deflection distance in free space[24]. Because $d/L_D = u_y/u_z$, the deflection velocity on exiting the field region then can be reconstructed from

$$u_y = -\frac{u_z}{L_D} \int_{y_0}^{y} \delta n/n_0 \,\mathrm{d}y, \tag{2}$$

where u_z is the initial velocity of the proton in the z direction and y_0 is the spatial boundary of $\delta n/n_0$ along the y direction on the detection plane.

It is necessary to mention that the impact of the electric field on the probe proton, which is mainly due to the space charge effect between the current filaments, has been experimentally proved to be negligible when compared with that of the magnetic field[17, 18]. In this paper, the influence of the electric field is also not taken into consideration.

3. Energy spectrum of the magnetic field and deflection velocity

In fluid physics, the velocity autocorrelation tensor is a commonly used tool to deduce the energy spectrum of three-dimensional fluid turbulence[26]. In analyzing three-dimensionally isotropic and stochastic magnetic turbulence, the autocorrelation tensor of the turbulent magnetic field is also useful in obtaining the energy spectrum of the magnetic field[20]. In this paper, the autocorrelation tensor of the two-dimensionally isotropic, stochastic and static magnetic field $\boldsymbol{B}$ is defined as

$$R_{ij}(\boldsymbol{p},\boldsymbol{p}') = \left\langle \boldsymbol{B}_i(\boldsymbol{p})\boldsymbol{B}_j(\boldsymbol{p}')\right\rangle, \tag{3}$$

where the subscripts i and j stand for x or z, $\boldsymbol{p}$ and $\boldsymbol{p}'$ are two arbitrary positions on the x–z plane, and the bracket $\langle\ \rangle$ stands for the mean operator. Because of the isotropy of the magnetic field in the x–z plane, $R_{ij}(\boldsymbol{p},\boldsymbol{p}')$ can be written as a function of the displacement vector $\boldsymbol{r} = \boldsymbol{p} - \boldsymbol{p}' = r_x\boldsymbol{e}_x + r_z\boldsymbol{e}_z$ using $R_{ij}(\boldsymbol{r})$. The two-dimensional Fourier transform of $R_{ij}(\boldsymbol{r})$ is

$$\hat{R}_{ij}(\boldsymbol{k}) = \frac{1}{(2\pi)^2}\iint R_{ij}(\boldsymbol{r})e^{-i\boldsymbol{k}\cdot\boldsymbol{r}}\,\mathrm{d}^2\boldsymbol{r}, \tag{4}$$

where $\boldsymbol{k} = k_x\boldsymbol{e}_x + k_z\boldsymbol{e}_z$. The inverse Fourier transform of $\hat{R}_{ij}(\boldsymbol{k})$ is

$$R_{ij}(\boldsymbol{r}) = \iint \hat{R}_{ij}(\boldsymbol{k})e^{i\boldsymbol{k}\cdot\boldsymbol{r}}\mathrm{d}^2\boldsymbol{k}. \tag{5}$$

Defining an autocorrelation function $R(\boldsymbol{r})$ with the trace of the autocorrelation tensor,

$$R(\boldsymbol{r}) = R_{ii}(\boldsymbol{r}) = R_{xx}(\boldsymbol{r}) + R_{zz}(\boldsymbol{r}). \tag{6}$$

In this paper, the subscript ii means that the Einstein summation convention is used. Because of the isotropy, $R_{xx}(\boldsymbol{r}) = R(\boldsymbol{r})/2$. Clearly, when $\boldsymbol{r} = 0$, $R(\boldsymbol{r} = 0)$ actually stands for the mean energy of the magnetic field, i.e., $B^2_{\mathrm{rms}} = \langle|\boldsymbol{B}_x|^2 + |\boldsymbol{B}_y|^2\rangle$. The subscript rms is an abbreviation for root mean square. Substituting Equation (5) into Equation (6) and letting $\boldsymbol{r} = 0$ yields

$$R(\boldsymbol{r} = 0) = \int_0^{2\pi}\int_0^{\infty}\hat{R}_{ii}(k)\,\mathrm{d}k\cdot k\,\mathrm{d}\varphi, \tag{7}$$

where φ is the polar angle in the $\boldsymbol{k}$ plane. Under the assumption of two-dimensional isotropy, Equation (7) can be rewritten as

$$R(\boldsymbol{r} = 0) = \int_0^{\infty} 2\pi k\hat{R}_{ii}(k)\,\mathrm{d}k. \tag{8}$$

Considering that $R(\boldsymbol{r} = 0)$ corresponds to the magnetic field energy, the integrand $2\pi k\hat{R}(k)$ actually is the energy spectrum of the magnetic field, and is denoted by

$$E_B(k) = 2\pi k\hat{R}(k), \tag{9}$$

where $\hat{R}(k) = \hat{R}_{ii}(k)$. Letting $k = k_x$ and $k_z = 0$, we have

$$E_B(k_x) = 2\pi k_x\hat{R}(k_x, k_z = 0). \tag{10}$$

Similar to the definition of $R_{ij}(\boldsymbol{p},\boldsymbol{p}')$, the autocorrelation tensor of the deflection velocity $\boldsymbol{u}$ is defined as

$$M_{ij}(\boldsymbol{p},\boldsymbol{p}') = \left\langle \boldsymbol{u}_i(\boldsymbol{p})\boldsymbol{u}_j(\boldsymbol{p}')\right\rangle. \tag{11}$$

Substituting Equation (1) into Equation (11) gives

$$M_{yy}(r_x) = \left(\frac{q}{\gamma m_p}\right)^2\int_0^{l_z}\mathrm{d}z\int_0^{l_z}\mathrm{d}z' R_{xx}(\boldsymbol{r}). \tag{12}$$

Letting $r_z = z - z'$, we get

$$M_{yy}(r_x) = l_z\left(\frac{q}{\gamma m_p}\right)^2\int_{-z}^{l_z - z}\mathrm{d}r_z R_{xx}(\boldsymbol{r}). \tag{13}$$

Because at the outside region of the magnetic field, $R_{xx}(\boldsymbol{r}) \approx 0$, the upper and lower integral limits in Equation (13) can be extended to $(-\infty, \infty)$ approximately. After substituting $R_{xx}(\boldsymbol{r}) = R(\boldsymbol{r})/2$ into Equation (13), we have

$$M_{yy}(r_x) = \frac{l_z}{2}\left(\frac{q}{\gamma m_p}\right)^2\int_{-\infty}^{\infty}\mathrm{d}r_z R(\boldsymbol{r}). \tag{14}$$

Equation (14) builds a relationship between the autocorrelation tensors of the two-dimensional magnetic field and the one-dimensional deflection velocity. The one-dimensional Fourier transforms of the left- and right-hand sides of Equation (14) give

$$\text{left}: \hat{M}_{yy}(k_x) = \frac{1}{2\pi}\int_{-\infty}^{\infty}M_{yy}(r_x)e^{-ik_x\cdot r_x}\,\mathrm{d}r_x \tag{15}$$

and

$$\text{right}: \pi l_z\left(\frac{q}{\gamma m_p}\right)^2\hat{R}(k_x, k_z = 0), \tag{16}$$

where Equation (16) has been written as a two-dimensional Fourier transform form of $R(r_x, r_z)$ by letting $k_z = 0$.

By rewriting $\hat{M}_{yy}(k_x)$ as $E_u(k_x)$, we get

$$E_u(k_x) = \pi l_z \left(\frac{q}{\gamma m_p}\right)^2 \hat{R}(k_x, k_z = 0). \tag{17}$$

The inverse Fourier transform of $\hat{M}_{yy}(k_x)$ has the form

$$M_{yy}(r_x) = \int \hat{M}_{yy}(k_x) e^{ik_x r_x} \, \mathrm{d}k_x. \tag{18}$$

At the same time, according to Parseval's theorem in the one-dimensional case, it gives that

$$2\pi \int \hat{u}_y^2(k) \, \mathrm{d}k_x = \int u_y^2(x) \, \mathrm{d}x \approx \langle u_y^2(x) \rangle l_x, \tag{19}$$

where $\hat{u}_y(k_x) = (1/2\pi) \int u_y(x) e^{-ik_x x} \, \mathrm{d}x$.

From $M_{yy}(r_x) = \langle \boldsymbol{u}_y(x) \boldsymbol{u}_y(x + r_x) \rangle$ we know that, if $r_x = 0$, $M_{yy}(r_x = 0) = \langle u_y^2(x) \rangle$. Thus, by letting $r_x = 0$ and substituting Equation (18) into Equation (19), we obtain

$$\int \hat{M}_{yy}(k_x) \, \mathrm{d}k_x = \frac{2\pi}{l_x} \int \hat{u}_y^2(k) \, \mathrm{d}k_x. \tag{20}$$

Clearly, $\hat{M}_{yy}(k_x) = (2\pi/l_x)\hat{u}_y^2(k_x)$. Then, the energy spectrum of the deflection velocity is deduced as

$$E_u(k_x) = \frac{2\pi}{l_x} \hat{u}_y^2(k_x). \tag{21}$$

4. Strength and wavelength of the magnetic field

By combining Equations (10), (17) and (21), we get

$$E_B(k_x) = \frac{4\pi}{l_z l_x} \left(\frac{\gamma m_p}{q}\right)^2 k_x \hat{u}_y^2(k_x), \tag{22}$$

which means that a relationship is built between the energy spectrum of the magnetic field and the spatial spectrum of the deflection velocity. When the spatial distribution of the one-dimensional deflection velocity $u_y(x)$ is obtained, the energy spectrum of the two-dimensionally isotropic and stochastic magnetic field can then be deduced. The method of obtaining $u_y(x)$ from proton radiography has been presented in Section 3.

The mean strength of the magnetic field is then acquired through

$$B_{\mathrm{rms}}^2 = \int_0^\infty \mathrm{d}k E_B(k_x). \tag{23}$$

The main spatial wavelength of $|\boldsymbol{B}|^2$, i.e., $\lambda_{|B|^2} = 2\pi/k_x$, can be read from the energy spectrum of the stochastic magnetic field $E_B(k_x)$. The main spatial wavelength of the magnetic field $|\boldsymbol{B}|$ then equals

$$\lambda_{|B|} = \lambda_{|B|^2}. \tag{24}$$

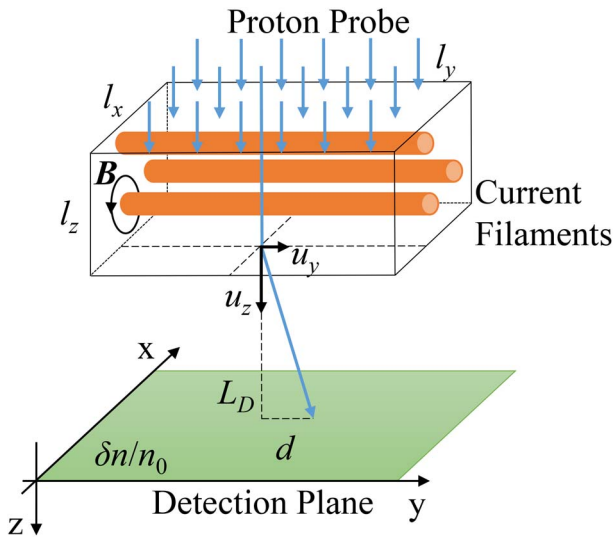

Figure 1. Schematic diagram of proton radiography of a two-dimensionally isotropic and stochastic magnetic field.

5. Numerical verification

In order to validate the above theory, numerical calculations based on ray tracing methods are conducted to simulate radiography of the Weibel-instability-generated two-dimensionally isotropic and stochastic magnetic field[24].

The three-dimensional magnetic field to be radiographed is pre-set as follows. Two hundred tube-like magnetic field structures are distributed in a cross-section of $l_x \times l_z = 0.8\ \mathrm{mm} \times 0.8\ \mathrm{mm}$ in the x–z plane, with the current filaments directed along the y direction, as shown in Figure 1. The field region in the y direction is from $y = 0\ \mathrm{mm}$ to $y = 4\ \mathrm{mm}$. According to the Biot–Savart law, the spatial distribution of each magnetic tube can be expressed as $\boldsymbol{B}_p = [B_0(r - r_0)/R_0] \exp[-(r - r_0)^2/R_0^2] \exp(-y^2/l_y^2)\boldsymbol{e}_\varphi$, where $r = \sqrt{x^2 + z^2}$, $\boldsymbol{e}_\varphi = \boldsymbol{e}_x + \boldsymbol{e}_y$, and R_0 and l_y denote the transversal and longitudinal lengths of the tube, respectively. The subscript p is an abbreviation for pre-set. B_0 is the amplitude of the magnetic field tube and r_0 is the transversal center position of each magnetic tube. For each magnetic tube, r_0 is randomly distributed in the transversal plane. According to previous experiments and the particle-in-cell simulations, B_0 and R_0 are set to be 10 T and 40 μm, respectively[18]. l_y is set to be 1.2 mm, which is long enough when compared to the transversal length of the magnetic tube. It allows us to regard the magnetic tube as being constantly distributed in the longitudinal direction, which, most importantly, suggests that the isotropy of the pre-set

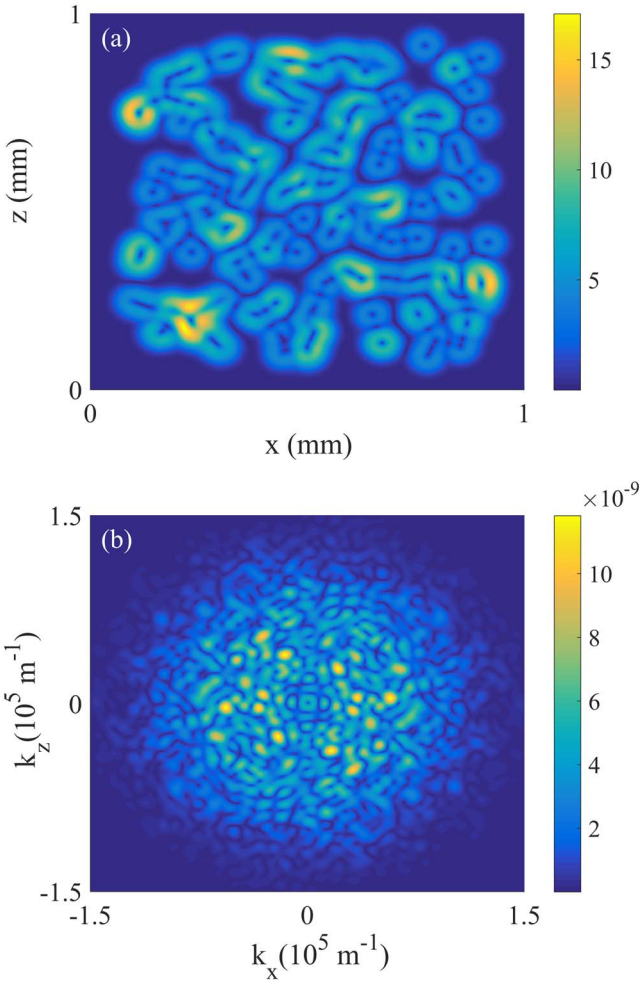

Figure 2. (a) Transversal cross-section of the pre-set stochastic magnetic field tubes at $y = 2$ mm. (b) Two-dimensional spectrum of the magnetic field by taking Fourier transforms of the field in (a), which shows an isotropic feature.

magnetic field is two-dimensional. These parameter settings correspond to the situation of a thermal anisotropy-driven Weibel instability during the process of plasma expanding into the vacuum[18].

The cross-section of the magnetic field strength at $y = 2$ mm is shown in Figure 2(a). The maximum strength is about 17 T. This is greater than B_0, which results from the spatial overlap of the magnetic tubes. In Figure 2(b), the two-dimensional distribution of the magnetic field in $\boldsymbol{k}$ space $\hat{B}_p(k_x, k_z) = \sqrt{|\hat{\boldsymbol{B}}_{xp}(k_x, k_z)|^2 + |\hat{\boldsymbol{B}}_{zp}(k_x, k_z)|^2}$ suggests that the magnetic field is approximately isotropic in the x–z plane, where $\hat{\boldsymbol{B}}_{xp}(k_x, k_z)$ and $\hat{\boldsymbol{B}}_{zp}(k_x, k_z)$ are the two-dimensional Fourier transforms of $\boldsymbol{B}_{xp}(x, z)$ and $\boldsymbol{B}_{zp}(x, z)$, respectively. The mean strength of the pre-set magnetic field $B_{\rm rmsp}$ can be acquired conveniently by making a spatial average of the magnetic field distribution $B_p(x, z) = \sqrt{|\boldsymbol{B}_{xp}(x, z)|^2 + |\boldsymbol{B}_{zp}(x, z)|^2}$ in the x–z plane,

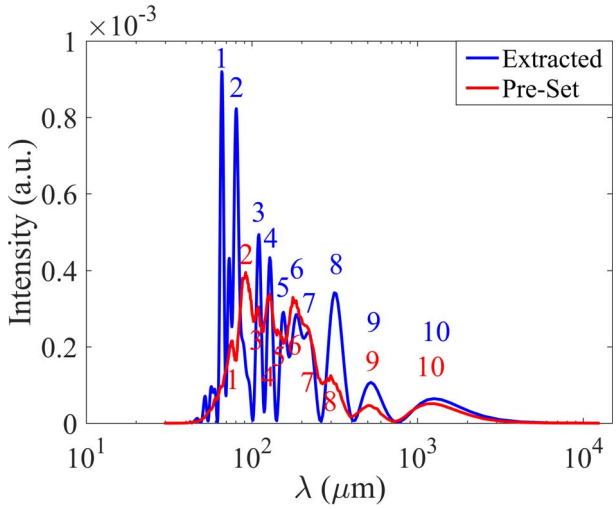

Figure 3. One-dimensional energy spectrum of the magnetic field $E_B(k)$. The red line corresponds to the energy spectrum obtained by taking Fourier transforms of the pre-set magnetic field in Figure 2(a), whereas the blue line corresponds to the energy spectrum extracted from proton radiography with Equation (22).

i.e., $B_{\rm rmsp} = (1/S)\iint B_p(x, z)\,{\rm d}x{\rm d}z$, where S is the transversal cross-sectional area of the magnetic field region. It is inferred from Figure 2(a) that $B_{\rm rmsp} \approx 4.51$ T.

The energy spectrum of the pre-set magnetic field in Figure 2(a), $E_{Bp}(k_x)$, can be acquired as follows. From the two-dimensional Parseval's theorem

$$\iint B^2(x, z)\,{\rm d}x\,{\rm d}z = 4\pi^2 \int |\hat{B}(k)|^2\,{\rm d}^2k, \qquad (25)$$

we know that $B^2_{\rm rmsp} = \int (8\pi^3/S)k|\hat{B}_p(k)|^2\,{\rm d}k$, where $\hat{B}_p(k)$ is the one-dimensional spectrum of the magnetic field in $k = \sqrt{k_x^2 + k_z^2}$ space and can be deduced from $\hat{B}_p(k_x, k_z)$ in Figure 2(b). According to Equation (9), the one-dimensional energy spectrum of the pre-set magnetic field is then given as $E_{Bp}(k) = (8\pi^3/S)k|\hat{B}_p(k)|^2$, shown as the red line in Figure 3. The blue line corresponds to the energy spectrum of the magnetic field extracted from the proton radiography, which will be described in detail later. Because of the isotropy, $E_{Bp}(k_x) = E_{Bp}(k)$. The mean strength of the pre-set magnetic field, when deduced from $E_{Bp}(k_x)$ by $B_{\rm rmsp} = \sqrt{\int_0^\infty {\rm d}k\,E_{Bp}(k_x)}$, is found to be $B_{\rm rmsp} \approx 4.51$ T, which is equal to the result obtained from the spatial averaging method previously. At the same time, the main wavelength of the pre-set magnetic field, which is taken from the highest peak on the energy spectrum of the pre-set magnetic field in Figure 3, is about $\lambda_{|B|p} = \lambda_{|B|^2p} \approx 86$ μm.

In this paper, our interest is limited to the case in which the Weibel instability is collisionless. In proton radiography of the Weibel-instability-generated magnetic field, the spatial density perturbation of the proton beam, which is introduced

from the magnetic field, is small enough to avoid the probe trajectory crossing or overlapping. Also, space charge effects between the probe protons are neglected. This allows the ray tracing method to be used to simulate the process of proton radiography of the magnetic field. In this paper, the kinetic energy of the mono-energy probe proton is 10 MeV, emitted parallel with the z direction from an extended proton source. The distance from the detection plane to the magnetic field region is $L_D = 5$ cm. The trajectories of the probe protons inside the field region are calculated with the Runge–Kutta algorithm. Outside of the field region, the probe protons drift during free flight before they reach the detection plane.

Numerical results show that after traversing the field region, the maximum proton deflection velocity in the y direction, $u_{y\max}$, is about 2.1×10^5 m/s. While in the x direction, the maximum deflection velocity, $u_{x\max}$, is about 1.5×10^2 m/s, which is about three orders of magnitude lower than $u_{y\max}$. This ensures the assumption of $\boldsymbol{u} \approx u_y \boldsymbol{e}_y$ in Equation (1). It also indicates that in proton radiography of a Weibel-instability-generated magnetic field, the proton density striations on the detection plane are mainly contributed by the longitudinal deflection velocity u_y, and the influence introduced to proton radiography by B_z is negligible.

Figure 4(a) shows the proton density perturbation on the detection plane. The spatial structures in Figure 4(a) are quite similar to the results in Figure 2 of the publication by Huntington *et al.*, which are obtained with both particle-in-cell simulations and experiments[17]. This also helps to support the model simplification in our paper.

From Figure 4(a) we can see that $\delta n/n_0 < 1$, which indicates that the linearity requirement is satisfied and trajectory crossings or overlappings between the protons do not happen under our chosen spatial resolution[24]. It allows us to reconstruct the deflection velocity at the exit of the field region from the density perturbation in Figure 4(a) with Equation (2). The spatial distribution of the reconstructed deflection velocity u_{ye} is shown in Figure 4(b). The one-dimensional distribution of the extracted u_{ye} at $y = 2$ mm is shown as the blue line in Figure 4(c), which is almost coincident with the deflection velocity integrated from Equation (1) with the pre-set magnetic field, shown as the red line in Figure 4(c). In order to distinguish them from the pre-set values of the magnetic field, the results extracted from the proton density perturbation are all subscripted with e as an abbreviation for extracted. The perfect agreement between the two deflection velocities is due to two reasons. Firstly, the low-density perturbation in Figure 4(a) indicates that the trajectory crossings of the probe protons are sufficiently prevented under the chosen spatial resolution. Secondly, the density perturbation is almost invisible at the exit of the field region (not shown), i.e., $\delta n/n_0 \approx 0$. This indicates that the deflection distance inside the field region is negligible and ensures that the assumption of collimation of the proton trajectories in deriving Equation (1) is valid. In other situations when the maximum of $\delta n/n_0$ approaches 1 or

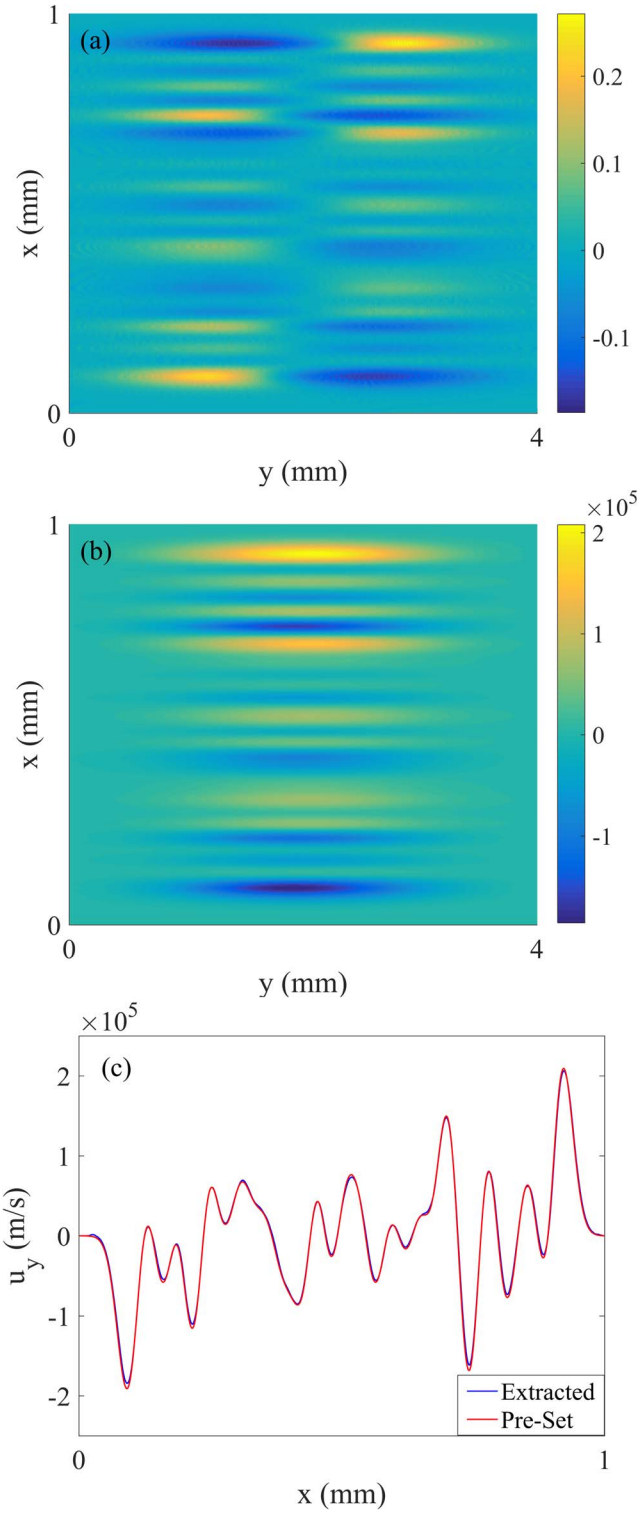

Figure 4. (a) Proton density perturbation $\delta n/n_0$ on the detection plane when $L_D = 5$ cm. (b) The extracted two-dimensional distribution of u_y. (c) One-dimensional distributions of u_y at $y = 2$ mm from the extracted results and the pre-settings.

even higher, or the deflection distance inside the field region is too large to be ignored, the differences between the two deflection velocities in Figure 4(c) could be more evident[24].

$\hat{u}_{ye}(k_x)$ is obtained by taking the Fourier transform of the deflection velocity $u_{ye}(x)$ in Figure 4(c). The extracted one-dimensional energy spectrum of the magnetic field $E_{Be}(k_x)$ is then obtained by substituting $\hat{u}_{ye}(k_x)$ into Equation (22), i.e., $E_B(k_x) = (4\pi/l_z l_x)(\gamma m_p/q)^2 k_x \hat{\boldsymbol{u}}_y^2(k_x)$, shown as the blue line in Figure 3.

We can see from Figure 3 that the amplitude and the envelope shape of the extracted magnetic field energy spectrum are approximately equal to the pre-set ones. Ten peaks are found in the energy spectrum of the pre-set magnetic field, marked with red numbers in Figure 3, respectively. For every red peak, a corresponding peak with a very close wavelength can be found in the extracted energy spectrum, marked with blue numbers. For most regions of the magnetic energy spectrum, the red and blue lines have either close amplitudes (specifically refer to the regions around peaks 5, 6, 7, 9, 10) or close peak–valley-averaged amplitudes (specifically refer to regions around peaks 1, 2, 3, 4, 8). This validates the use of Equation (22).

In the extracted spectrum, peaks 1 and 2 have close wavelengths and evidently higher amplitudes when compared to the other peaks in the blue line. Therefore, the extracted main wavelength for the magnetic energy is taken from the average wavelength of peaks 1 and 2. The result shows that $\lambda_{|B|^2 e} \approx 74\ \mu\text{m}$. According to Equation (24), the main wavelength for the magnetic field then equals $\lambda_{|B|e} \approx 74\ \mu\text{m}$. This extracted value is quite close to the pre-set one, i.e., $\lambda_{|B|p} \approx 86\ \mu\text{m}$. The extracted mean strength of the magnetic field is calculated by Equation (23) with the blue energy spectrum in Figure 3. It gives $B_{r\text{mse}} \approx 5.08$ T, which agrees well with the pre-set value, i.e., $B_{\text{rmsp}} \approx 4.51$ T.

It is necessary to mention that our theoretical analyses predict that the energy spectra are strictly equal for an ideal stochastic magnetic field; the difference between the two energy spectra in Figure 3 could be the result of a lack of stochasticity of the magnetic field. For an ideal stochastic distribution, the spectrum obtained from the Fourier transforms could be very smooth. However, the spectrum obtained from our pre-set magnetic field in Figure 2(a) shows ten small peaks over the large envelope, which indicates that the magnetic field distribution is not an ideal one. Actually, the stochastic fields in our simulations are generated with two hundred randomly distributed magnetic field tubes of the same magnitude and structure. It is hard to build an ideal stochastic field with those tubes. That is the reason which leads to the small differences between $B_{r\text{mse}} \approx 5.08$ T and $B_{\text{rmsp}} \approx 4.51$ T, and between $\lambda_{|B|e} \approx 74\ \mu\text{m}$ and $\lambda_{|B|p} \approx 86\ \mu\text{m}$. Nevertheless, the matching of the positions of the ten peaks and the clearly seen envelope on the spectra all indicates that the magnetic field is still a stochastic one, though not an ideal one.

Comprehensively examining the consistency between the pre-set values and the extracted results, we conclude that the method demonstrated above is applicable for extracting the main wavelength and mean strength of the Weibel-instability-generated magnetic field with proton radiography.

6. Discussion

In the above demonstration, some ideal model simplifications are assumed. The situations in experiment, however, could be much more complicated.

In this paper, all the probe protons have the same kinetic energy and are emitted from the source at the same time. Experimentally, the proton probes used in the radiography are mostly generated through the target normal sheath acceleration mechanism. The difference in the proton emission time and energy spread can broaden the probe duration. Generally, the probe pulse duration can reach about one picosecond[27]. Also, the amplitudes and spatial structures of the magnetic field may not be static, and could change during the growth of the Weibel instability[13]. The extracted strength and wavelength are actually time-averaged results of the real ones. When the magnetic field evolves slowly during the passage of the proton probe, the strength and wavelength extraction method demonstrated above could yield time resolution using radiochromatic film stacks as the proton detector. However, if the magnetic field evolves rapidly during the passage of the proton probe, the extraction method will fail. This should be noticed especially in the growth stage of the Weibel instability and when the Weibel instability growth rate is large. Nevertheless, this strength and wavelength extraction method for the Weibel-instability-generated magnetic field is mostly capable after saturation of the instability. For an ion-driven Weibel instability, the magnetic field duration can be as long as several nanoseconds after it has been stimulated, and the probe pulse duration of several picoseconds has a negligible impact on the time resolution of the radiography[14]. For Weibel instability driven by electron thermal anisotropy, mostly investigated with an expanding plasma in the interaction of a laser pulse with a solid target, the magnetic field duration after saturation can also reach the range of several tens of picoseconds, which is also large enough to neglect the influence introduced by the probe pulse duration[15].

At the same time, as has been discussed in Section 4, this extraction method is based on the assumption of two-dimensional isotropy and stochasticity of the magnetic field. However, in some circumstances, this assumption cannot be ensured and the magnetic field strength and wavelength extraction method demonstrated above may fail. For example, at the end of the nonlinear stage of the Weibel instability, merging of the current filaments is serious. There could be only several current filaments remaining, in which case

two-dimensional isotropy and stochasticity are no longer fulfilled. Nevertheless, under such cases, the Faraday rotation method is capable of inferring the magnetic field strength and has been successfully applied in experiments[28].

7. Conclusion

A method to infer the strength and wavelength of the Weibel-instability-generated magnetic field from the proton radiography has been demonstrated in our paper. With theoretical analyses, it is found that in the proton radiography of a Weibel-instability-induced magnetic field, which is usually two-dimensionally isotropic and stochastic, the proton flux density perturbation on the detection plane can be related to the energy spectrum of the magnetic field. It further allows us to obtain the mean strength and main wavelength of the magnetic field. Using ray tracing methods, a proton beam has been emitted numerically to simulate radiography of a two-dimensionally isotropic and stochastic magnetic field with the pre-set main wavelength equal to approximately 86 μm and the pre-set mean strength equal to approximately 4.51 T. With our extraction method, the main wavelength and mean strength of the magnetic field, when inferred from the detected proton density perturbation, are about 74 μm and 5.08 T, respectively. The consistency between the pre-set values and the extracted results suggests that, through the extraction method demonstrated in our paper, the mean strength and main wavelength of the two-dimensionally isotropic and stochastic magnetic field can be inferred well from proton radiography. This could be helpful in first experimental measurements of the strength and wavelength of the Weibel-instability-generated stochastic magnetic field.

Acknowledgements

This work was supported by the Science Challenge Project (No. TZ2016005), the National Natural Science Foundation of China (Nos. 11575030 and U1730449 (NSAF)) and the National Key Programme for S&T Research and Development in China (No. 2016YFA0401100).

References

1. E. S. Weibel, Phys. Rev. Lett. **2**, 83 (1959).
2. B. D. Fried, Phys. Fluids **2**, 337 (1959).
3. W. Fox, G. Fiksel, A. Bhattacharjee, P. Y. Chang, K. Germaschewski, S. X. Hu, and P. M. Nilson, Phys. Rev. Lett. **111**, 225002 (2013).
4. R. Jung, J. Osterholz, K. Lowenbruck, S. Kiselev, G. Pretzler, A. Pukhov, O. Willi, S. Kar, M. Borghesi, W. Nazarov, S. Karsch, R. Clarke, and D. Neely, Phys. Rev. Lett. **94**, 195001 (2005).
5. F. Fiuza, R. A. Fonseca, J. Tonge, W. B. Mori, and L. O. Silva, Phys. Rev. Lett. **108**, 235004 (2012).
6. A. Gruzinov and E. Waxman, Astrophys. J. **511**, 852 (1999).
7. C. Ren, M. Tzoufras, F. S. Tsung, W. B. Mori, S. Amorini, R. A. Fonseca, L. O. Silva, J. C. Adam, and A. Heron, Phys. Rev. Lett. **93**, 185004 (2004).
8. Y. Sentoku, K. Mima, P. Kaw, and K. Nishikawa, Phys. Rev. Lett. **90**, 155001 (2003).
9. Q. Jia, H. B. Cai, W. W. Wang, S. P. Zhu, Z. M. Sheng, and X. T. He, Phys. Plasmas **20**, 032113 (2013).
10. Q. Jia, K. Mima, H. B. Cai, T. Taguchi, H. Nagatomo, and X. T. He, Phys. Rev. E **91**, 023107 (2015).
11. B. Hao, W. J. Ding, Z. M. Sheng, C. Ren, X. Kong, J. Mu, and J. Zhang, Phys. Plasmas **19**, 072709 (2012).
12. A. Stockem, M. E. Dieckmann, and R. Schlickeiser, Plasma Phys. Control. Fusion **51**, 075014 (2009).
13. A. Stockem, T. Grismayer, R. A. Fonseca, and L. O. Silva, Phys. Rev. Lett. **113**, 105002 (2014).
14. M. Tzoufras, C. Ren, F. S. Tsung, J. W. Tonge, W. B. Mori, M. Fiore, R. A. Fonseca, and L. O. Silva, Phys. Rev. Lett. **96**, 105002 (2006).
15. C. Thaury, P. Mora, A. Héron, J. C. Adam, and T. M. Antonsen, Phys. Rev. E **82**, 026408 (2010).
16. N. L. Kugland, D. D. Ryutov, P. Y. Chang, R. P. Drake, G. Fikse, D. H. Froula, S. H. Glenzer, G. Gregori, M. Grosskopf, M. Koenig, Y. Kuramitsu, C. Kuranz, M. C. Levy, E. Liang, J. Meinecke, F. Miniati, T. Morita, A. Pelka, C. Plechaty, R. Presura, A. Ravasio, B. A. Remington, B. Reville, J. S. Ross, Y. Sakawa, A. Spitkovsky, H. Takabe, and H. S. Park, Nat. Phys. **8**, 809 (2012).
17. C. M. Huntington, F. Fiuza, J. S. Ross, A. B. Zylstra, R. P. Drake, D. H. Froula, G. Gregori, N. L. Kugland, C. C. Kuranz, M. C. Levy, C. K. Li, J. Meinecke, T. Morita, R. Petrasso, C. Plechaty, B. A. Remington, D. D. Ryutov, Y. Sakawa, A. Spitkovsky, H. Takabe, and H. S. Park, Nat. Phys. **11**, 173 (2015).
18. K. Quinn, L. Romagnani, B. Ramakrishna, G. Sarri, M. E. Dieckmann, P. A. Wilson, J. Fuchs, L. Lancia, A. Pipah, T. Toncian, O. Willi, R. J. Clarke, M. Notley, A. Macchi, and M. Borghesi, Phys. Rev. Lett. **108**, 135001 (2012).
19. N. L. Kugland, D. D. Ryutov, C. Plechaty, J. S. Ross, and H. S. Park, Rev. Sci. Instrum. **83**, 101301 (2012).
20. A. F. A. Bott, C. Graziani, P. Tzeferacos, T. G. White, D. Q. Lamb, G. Gregori, and A. A. Schekochihin, J. Plasma Phys. **83**, 905830614 (2017).
21. C. Graziani, P. Tzeferacos, D. Q. Lamb, and C. K. Li, Rev. Sci. Instrum. **88**, 123507 (2017).
22. P. Tzeferacos, A. Rigby, A. F. A. Bott, A. R. Bell, R. Bingham, A. Casner, F. Cattaneo, E. M. Churazov, J. Emig, F. Fiuza, C. B. Forest, J. Foster, C. Graziani, J. Katz, M. Koenig, C. K. Li, J. Meinecke, R. Petrasso, H. S. Park, B. A. Remington, J. S. Ross, D. Ryu, D. Ryutov, T. G. White, B. Reville, F. Miniati, A. A. Schekochihin, D. Q. Lamb, D. H. Froula, and G. Gregori, Nat. Commun. **9**, 591 (2018).
23. A. Karmakar, N. Kumar, G. Shvets, O. Polomarov, and A. Pukhov, Phys. Rev. Lett. **101**, 255001 (2008).
24. B. Du and X. F. Wang, AIP Adv. **8**, 125328 (2018).
25. C. J. Zhang, J. F. Hua, Y. Wan, C. H. Pai, B. Guo, J. Zhang, Y. Ma, F. Li, Y. P. Wu, H. H. Chu, Y. Q. Gu, X. L. Xu, W. B. Mori, C. Joshi, J. Wang, and W. Lu, Phys. Rev. Lett. **119**, 064801 (2017).
26. P. A. Davidson, *Turbulence* (Oxford University Press, Oxford, 2004).
27. A. Macchi, M. Borghesi, and M. Passoni, Rev. Mod. Phys. **85**, 751 (2013).
28. S. Y. Zhou, Y. F. Bai, Y. Tian, H. Y. Sun, L. H. Cao, and J. S. Liu, Phys. Rev. Lett. **121**, 255002 (2018).